nature portfolio

https://doi.org/10.1038/s41566-021-00922-8

Supplementary information

Magnetic on–off switching of a plasmonic laser

In the format provided by the authors and unedited

nature portfolio

https://doi.org/10.1038/s41566-021-00922-8

Supplementary information

Magnetic on–off switching of a plasmonic laser

In the format provided by the authors and unedited

Magnetic on-off switching of a plasmonic laser

Francisco Freire-Fernández,[1,2] Javier Cuerda,[1] Konstantinos S. Daskalakis,[1,3] Sreekanth Perumbilavil,[1] Jani-Petri Martikainen,[1] Kristian Arjas,[1] Päivi Törmä,[1] and Sebastiaan van Dijken[1]

[1] *Department of Applied Physics, Aalto University School of Science, P.O. Box 15100, FI-00076 Aalto, Finland*
[2] *Department of Chemistry, Northwestern University, Evanston, Illinois 60208, United States*
[3] *Department of Mechanical and Materials Engineering, Faculty of Technology, University of Turku, 20014 Turun Yliopisto, Finland*

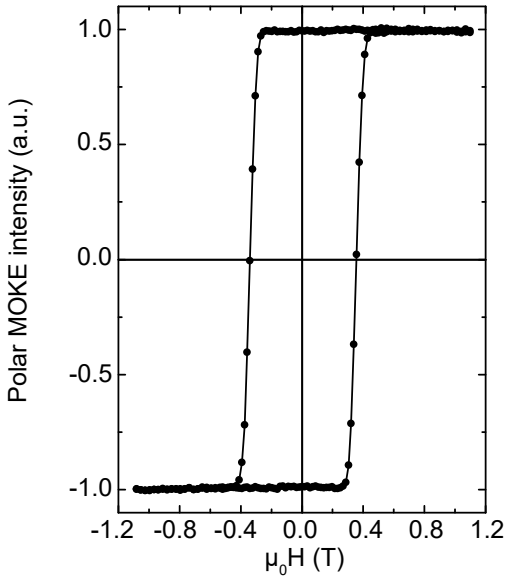

FIG. 1. Polar magneto-optical Kerr effect hysteresis loop of a square Co/Pt nanodot array on top of a Au(150)/SiO_2(20) bilayer. The nanodot diameter is 220 nm, its height is 68 nm, and the period of the array is 590 nm. The square hysteresis loop indicates that the Co/Pt nanodots are magnetized perpendicular to the sample plane. The saturation field is 0.44 T. In the experiments, we reverse the perpendicular magnetization of the Co/Pt nanodots by applying ±0.5 T fields.

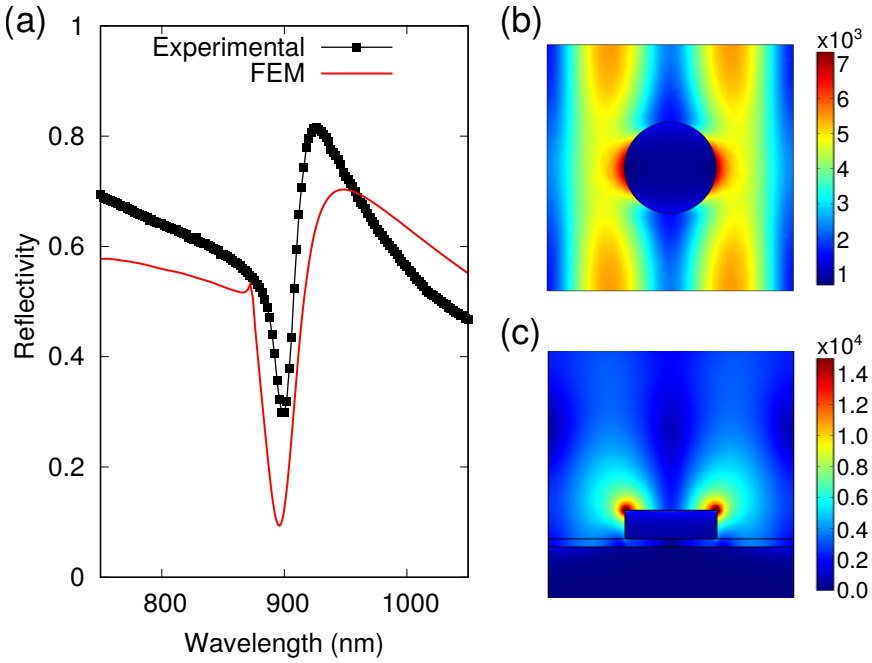

FIG. 2. Finite element method (FEM) simulation of a square lattice of Co/Pt nanodots on top of a Au(150)/SiO_2(20) bilayer. (a) Experimental and simulated reflectivity spectra for a square array with period $p_x = p_y = 590$ nm, nanodot diameter $D = 220$ nm, and height $h = 68$ nm. (b),(c) Simulated electric field distribution (amplitude $|\mathbf{E}(\mathbf{r})|/E_0$) at the wavelength corresponding to minimum reflectivity, for normal incident light with amplitude E_0 and linear polarization along the x-axis. The panels show (b) XY- and (c) XZ-planes intersecting the nanodot at mid-height ($z = 34$ nm) and across the center of the nanodot ($y = 0$ nm), respectively. The simulations are performed in Comsol Multiphysics software. Periodic boundary conditions along the x-axis and y-axis are implemented to simulate the response of an infinite nanodot array. A refractive index $n = 1.48$ is assumed for both the SiO_2 film and the uniform environment. Details on the FEM simulations are given in the Methods section.

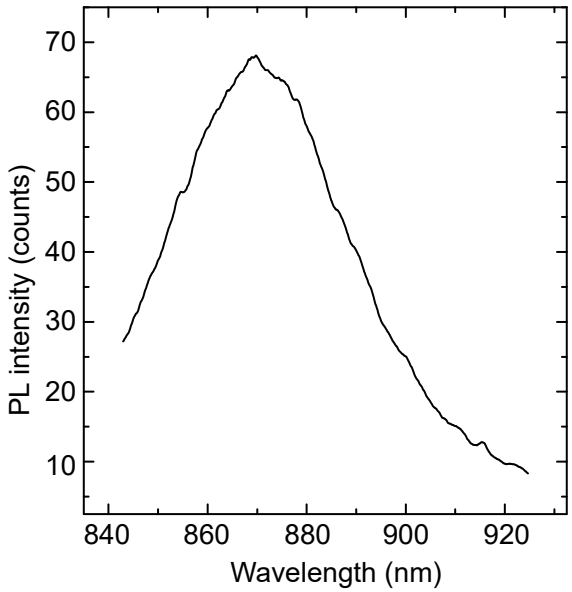

FIG. 3. Emission band of the 12 mM IR-140 dye solution used as the gain medium in the lasing experiments.

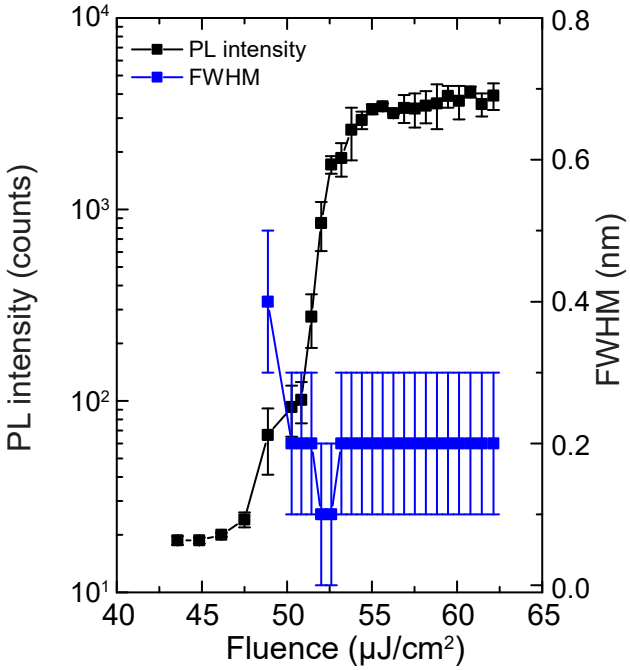

FIG. 4. PL intensity and FWHM of the lasing peak as a function of pump fluence for a square Co/Pt nanodot array on top of a Au(150)/SiO_2(20) bilayer under σ^- excitation. During the measurement, a +0.5 T magnetic field saturates the perpendicular magnetization of the Co/Pt nanodots up. At fluence values below 48.6 $\mu J/cm^2$, the background dye spontaneous emission is stronger than the PL of the SLR mode and hence, we cannot estimate its FWHM from these PL measurements.

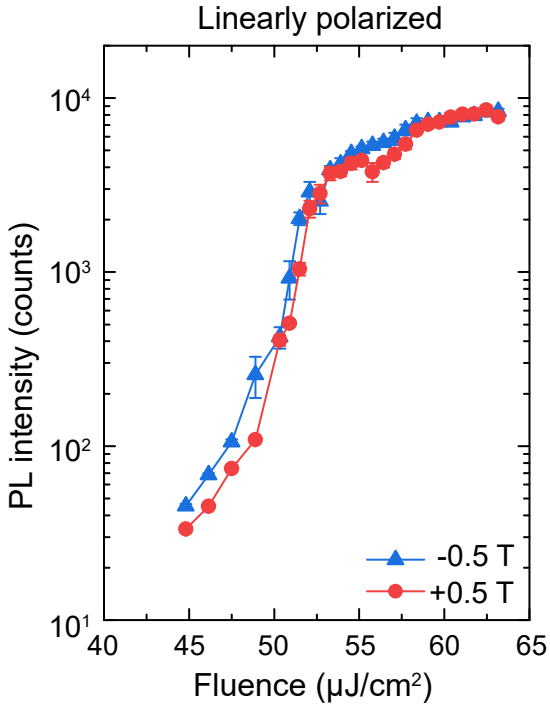

FIG. 5. PL intensity as a function of pump fluence for a square Co/Pt nanodot array on top of a Au(150)/SiO_2(20) bilayer under linearly polarized excitation. The nanodot diameter is 220 nm, its height is 68 nm, and the period of the array is 590 nm. The blue and red data are recorded with the magnetization of the Co/Pt nanodots pointing down and up, respectively. Contrary to circularly polarized excitation (Fig. 1(d),(e) in the main text), the lasing threshold and lasing intensity for linearly polarized pump pulses are the same for both magnetization directions within experimental error.

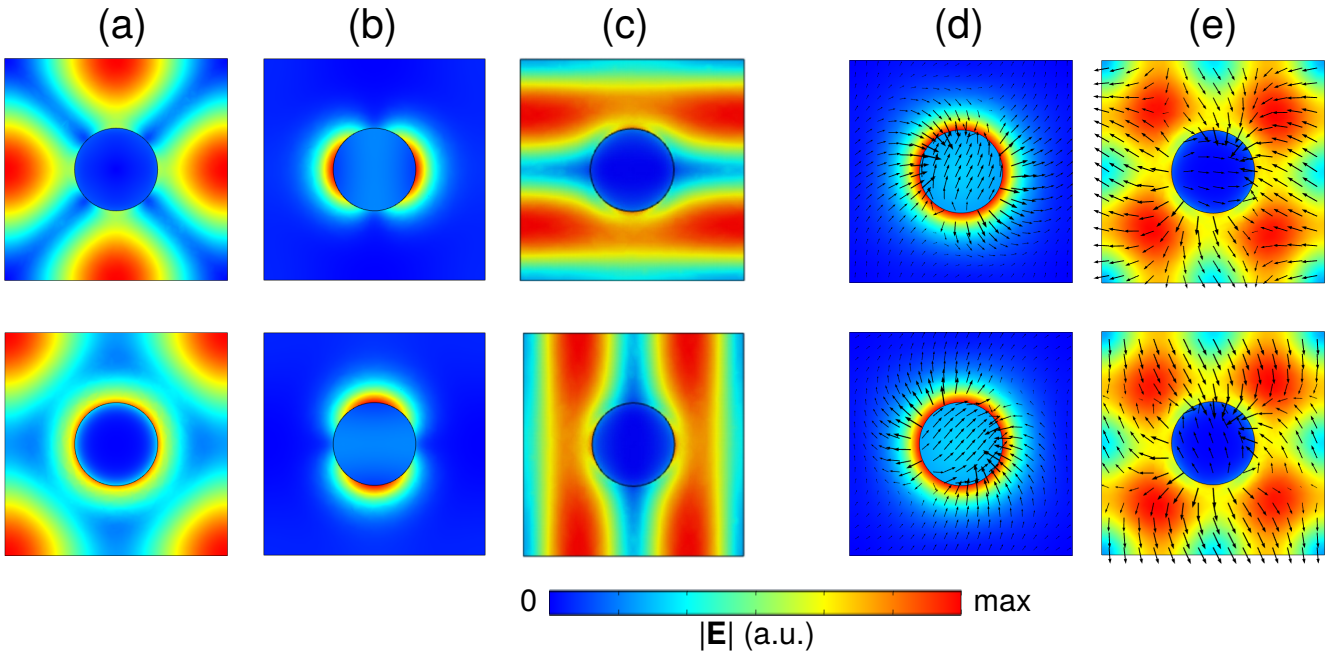

FIG. 6. Analysis of the modes sustained by the square lattice. (a)-(e) Eigenmodes resulting from FEM simulations. The electric field norm is shown for one unit cell at an XY-plane intersecting the nanodot at its mid-height. In the absence of a net magnetization, the lattice supports the modes shown in (a)-(c). When a net magnetization is simulated through nonzero off-diagonal terms in the permittivity tensor describing the optical response of the nanodots, the modes (b) and (c) transform into (d) and (e), respectively, whereas the modes in (a) remain unchanged. The modes in (a) located at 1.364 eV (wavelength 909 nm) with linewidth 0.016 eV (upper panel), and at 1.219 eV (wavelength 1017 nm) and linewidth 0.036 eV (lower panel) are dark in our experiment, because the symmetry of the field distribution at the lattice plane prevents the coupling to normal-incident far-field light polarized in that plane. The modes in (b) are doubly degenerate (due to the square lattice symmetry), and correspond to an in-plane hybrid mode at 0.982 eV (wavelength 1263 nm), with linewidth 0.255 eV. Panel (c) shows a doubly degenerate out-of-plane mode 1.384 eV (wavelength 896 nm) with linewidth 0.011 eV. The out-of-plane nature of this mode is revealed from its prominent E_z-component (not shown here). In the presence of non-zero magnetization, the doublet of panel (b) lifts its degeneracy and breaks down into modes at 0.976 eV (wavelength 1270 nm) with linewidth 0.259 eV (lower panel in (d)), and at 0.986 eV (wavelength 1257 nm) with linewidth 0.250 eV (upper panel in (d)). These modes correspond to the two broad peaks in Supplementary Fig. 7. Likewise, the doubly degenerate modes of (c) form the magnetized modes at 1.383 eV (wavelength 896.5 nm) with linewidth 0.011 eV (lower panel in (e)) and 1.384 eV (wavelength 895.8 nm) with linewidth 0.011 eV (upper panel in (e)), corresponding to the two narrow peaks in Supplementary Fig. 7. Arrows in panels (d) and (e) depict the vectorial electric field: $\mathbf{E} = (E_x, E_y)$, and show that the modes are different despite their similar field amplitude. Using the theoretical method introduced in the Methods section, we find that the mode pairs in panels (d) and (e) are circularly polarized, with σ^+ for the higher energy mode and with σ^- for the lower energy mode, in both cases, when the magnetization points up. Indeed, for the modes in (d) we find $|C_{\sigma^+}|^2 = 0.95$, $|C_{\sigma^-}|^2 = 0.10$ for the higher energy mode and $|C_{\sigma^-}|^2 = 0.95$, $|C_{\sigma^+}|^2 = 0.10$ for the lower energy mode. Likewise, we obtain $|C_{\sigma^+}|^2 = 0.96$, $|C_{\sigma^-}|^2 = 0.04$ for the higher energy mode in (e) and $|C_{\sigma^-}|^2 = 0.98$, $|C_{\sigma^+}|^2 = 0.02$ for the lower energy mode of that panel. The small numerical inaccuracies come from the calculation of the overlap integral of the field distributions (see Eq. (17) in the main text), due to finite size of the spatial discretization for the analyzed geometry.

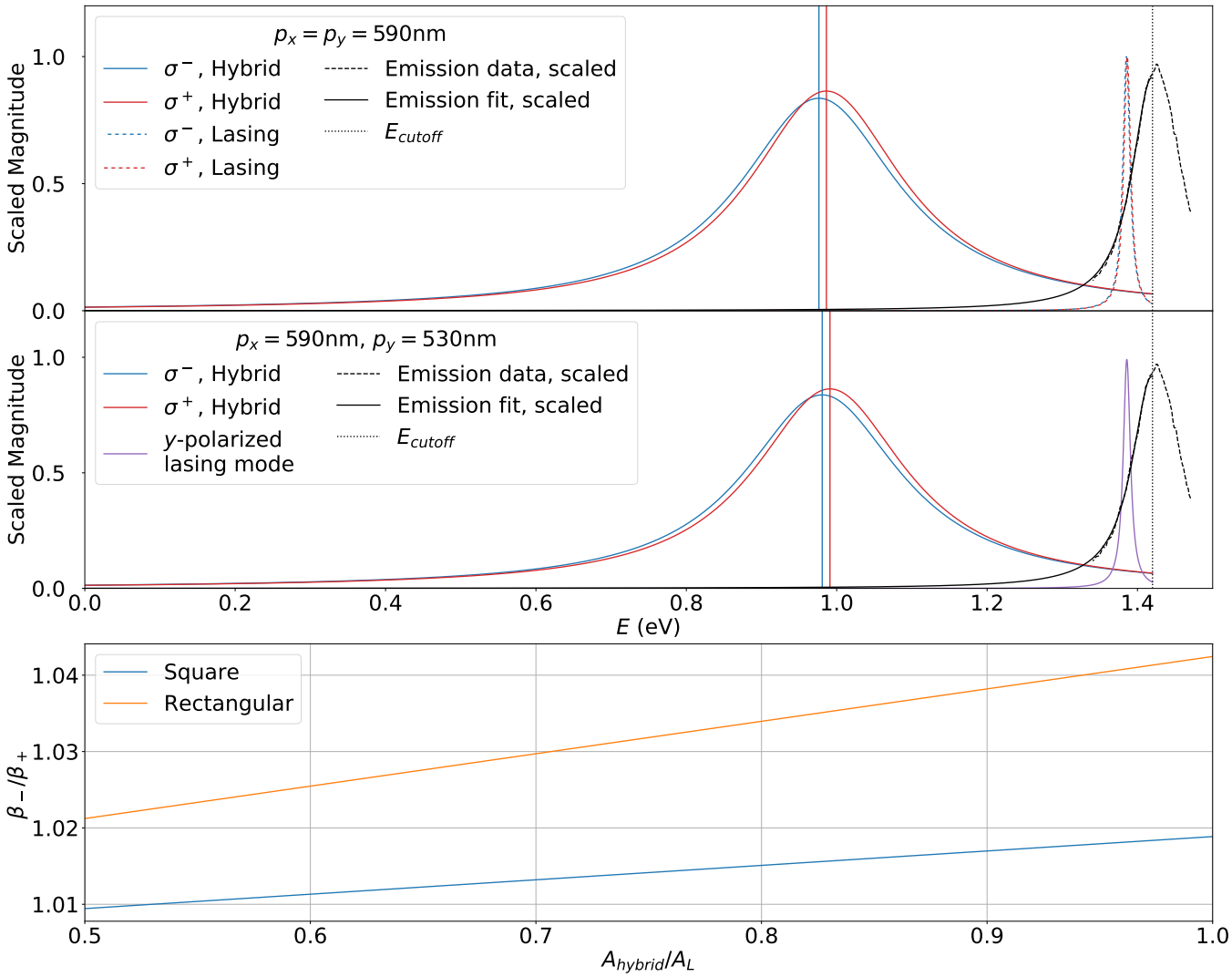

FIG. 7. The modes of square (top) and rectangular (middle) lattices along with the Lorentzian fit of the dye emission spectrum (top and middle). The modes are represented with Lorentzians whose center wavelength and linewidth are those of the eigenmodes obtained from FEM simulations; these are used as the absorption probabilities $\sigma(E)$ in the estimate of the β-factors, as explained in Methods. Here the approximately 0.5 nm splitting between the σ^- and σ^+ lasing modes around 1.38 eV is hardly visible, in contrast to the out-of-scale schematic of Fig. 3(c) in the main text, where it is exaggerated for visibility. As we only obtain the wavelengths and linewidths of the hybrid and lasing modes from the simulations, their relative magnitude is still arbitrary; their ratio A_{hybrid}/A_L remains an open parameter to be varied and affects the ratio of β-factors (bottom). In the calculations, absorption probabilities $\sigma(E)$ are scaled by A_{hybrid}/A_L with respect to the hybrid and lasing modes; the scaling is the same for the σ^- and σ^+ hybrid modes, so that it does not influence the chiral effect. Physically, the relative magnitude A_{hybrid}/A_L corresponds to the efficiency of light coupling to these modes in the near-field (relevant for the dye emission); from the lower panel we see the result is not highly sensitive to it. In the simulated reflectivity response of the system using far-field excitation, the hybrid mode peaks are about 60% of the lasing peaks; in the near-field regime, the coupling to the hybrid mode is expected to be similar or better, as the mode has very strong fields localized at the nanoparticles. Therefore, in our calculations we take the minimum A_{hybrid}/A_{SLR} to be 0.6. This gives a β-ratio range of 1.012 - 1.019 for the square and 1.025 - 1.042 for the rectangular lattice. The β-ratio is bigger for the rectangular lattice, consistent with the experimentally observed larger lasing threshold changes compared to the square lattice.

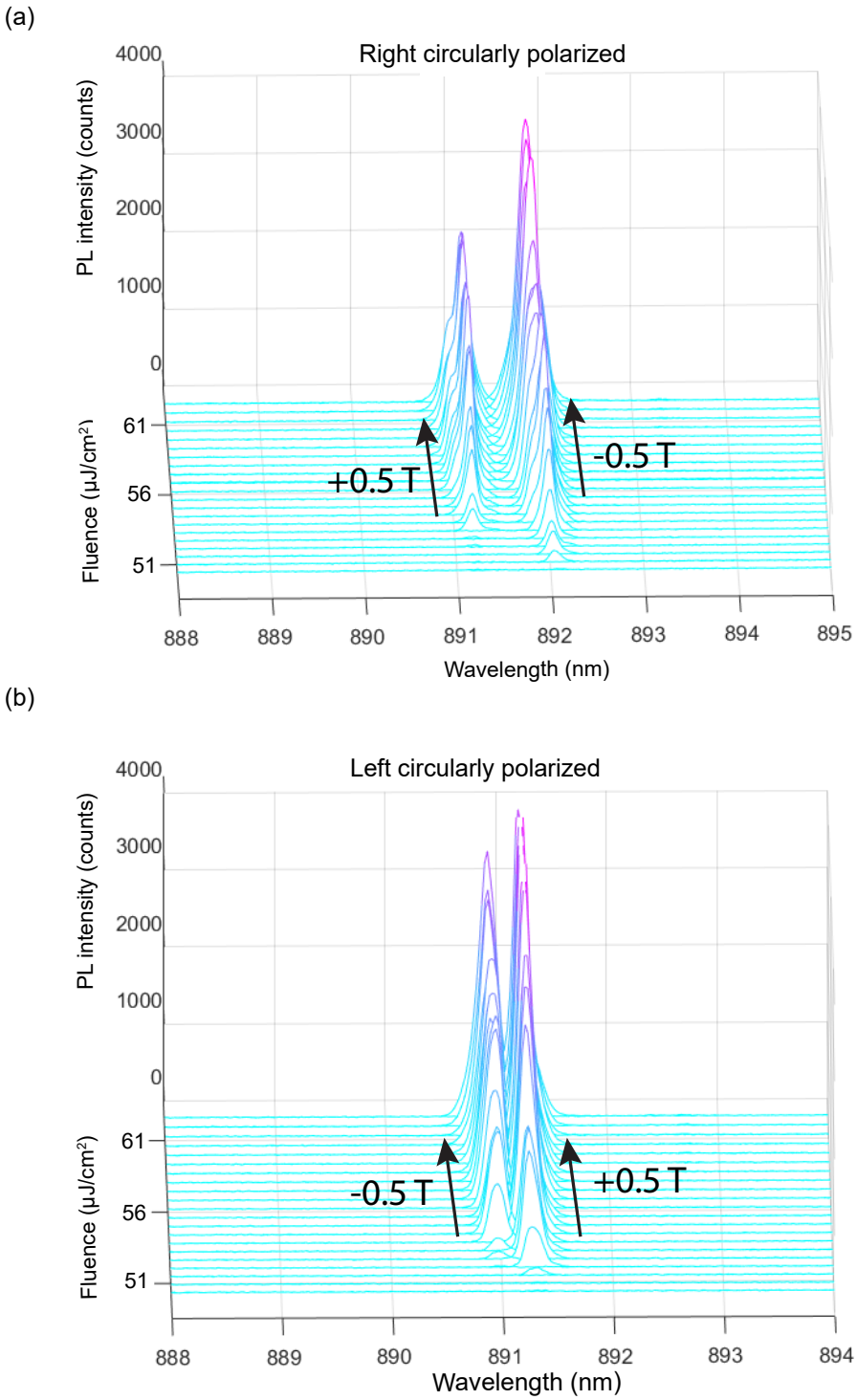

FIG. 8. PL intensity as a function of pump fluence, wavelength, and magnetic field corresponding to the data in Fig. 1(d),(e) in the main text. In panel (a), the fluence dependence of the lasing peak at lower wavelength is recorded in a +0.5 T magnetic field and the fluence dependence of the lasing peak at higher wavelength is recorded in a −0.5 T magnetic field. In panel (b), the fluence dependence of the lasing peak at lower wavelength is recorded in a −0.5 T magnetic field and the fluence dependence of the lasing peak at higher wavelength is recorded in a +0.5 T magnetic field.

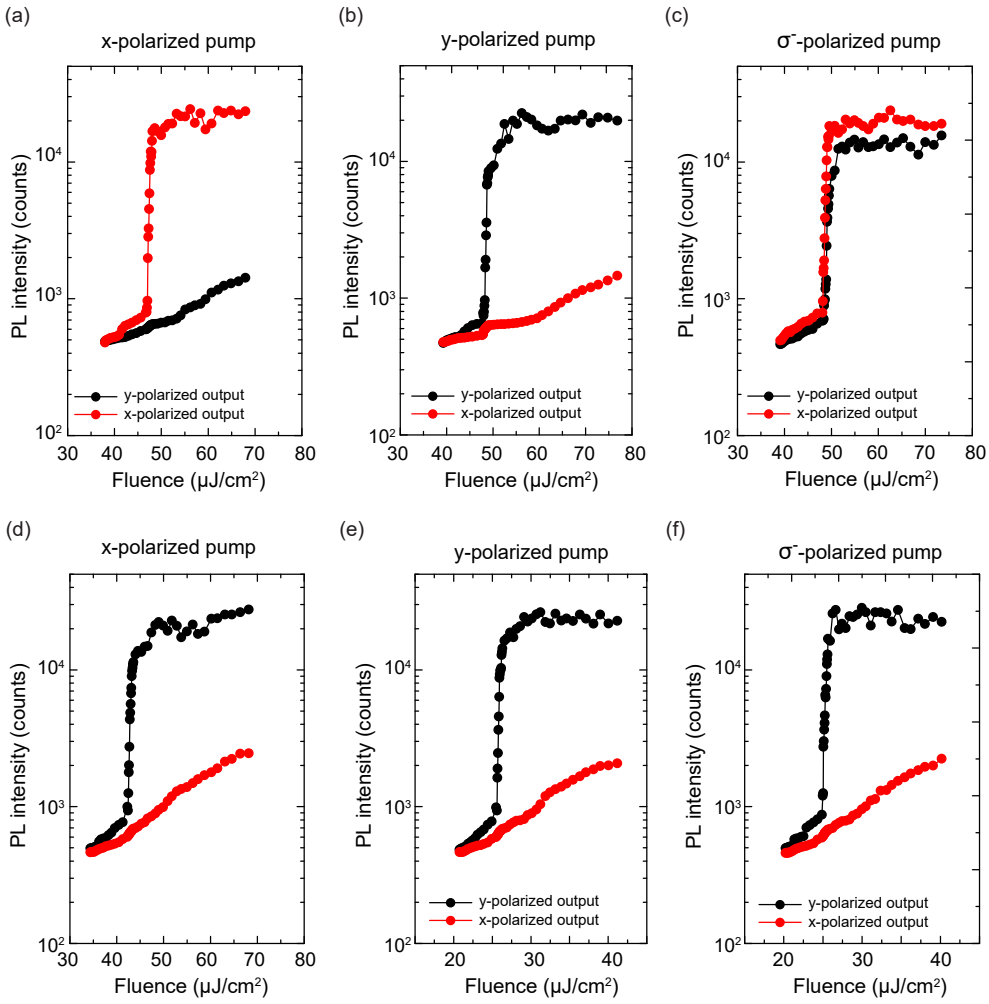

FIG. 9. Polarization of the lasing emission under linearly polarized excitation along the x- and y-axis and circularly polarized excitation with σ^- light. Panels (a)-(c) show experimental data for a square array with $p_x = p_y = 590$ nm and panels (d)-(f) depict measurement results for a rectangular array with $p_x = 590$ nm and $p_y = 530$ nm.

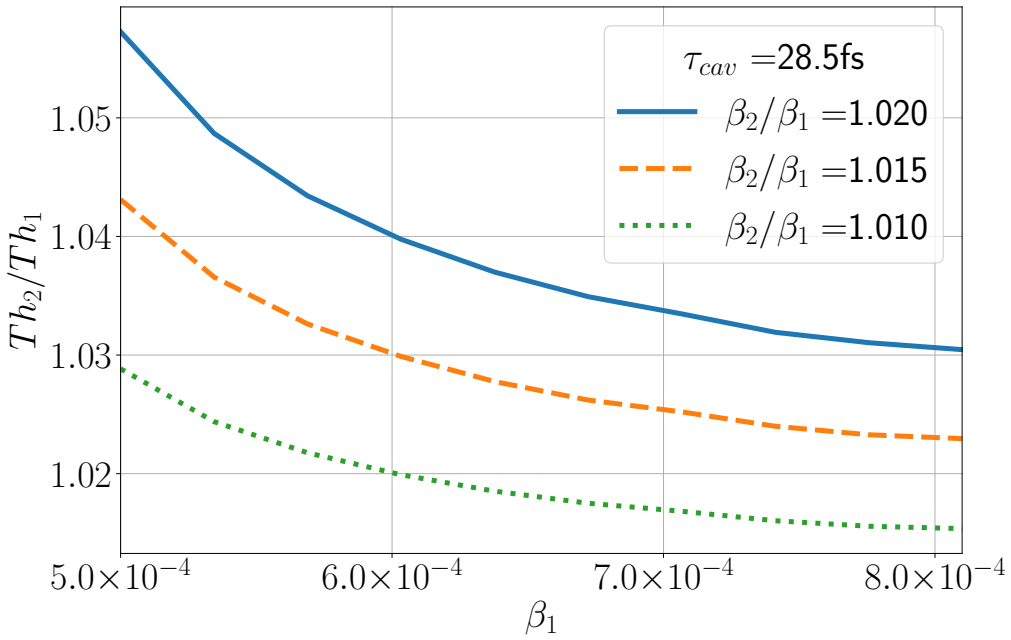

FIG. 10. Lasing threshold ratio, Th_2/Th_1, of two modes cavity lifetimes $\tau_{cav,1} = \tau_{cav,2} = 28.5$ fs and β-factors $\beta_{cav,1}$ and $\beta_{cav,2}$, as a function of $\beta_{cav,1}$. The lifetimes are given by the FEM simulations of the lasing modes in the square array (Supplementary Fig. 6(e)) and the lasing threshold is defined as the pump rate, r, where the integrated lasing signal crosses 1% of the highest calculated integrated signal (see rate equation analysis in Methods). A 1-2% change in the β-factor (as predicted for square lattice) results in a 2-4% threshold change for β-values in the order of $\beta \approx 6 \times 10^{-4}$. We have estimated the appropriate order of magnitude of the β-factor (it is the range used in this figure) from the ratio of the slopes below and above threshold in the experimental PL vs fluence curves. An example is given in Supplementary Fig. 11.

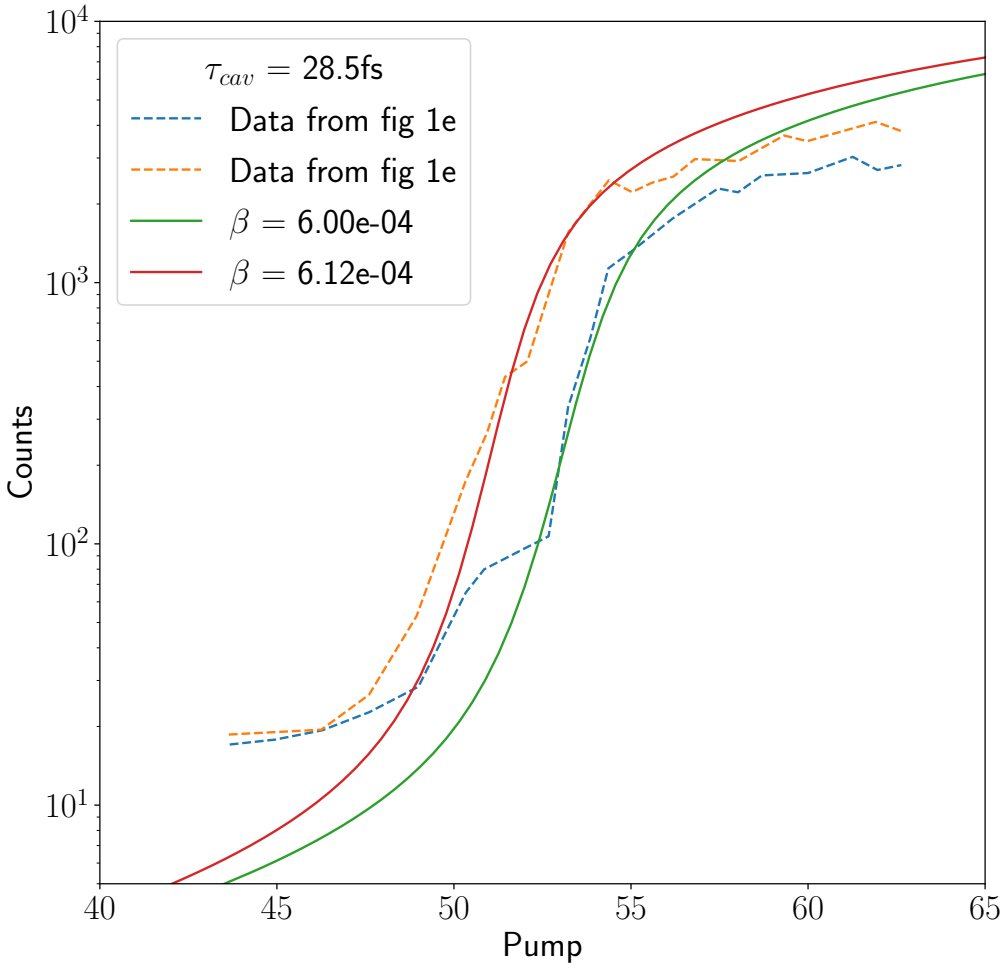

FIG. 11. Integrating Eq. (8) for different pump rates r gives the PL and thus a lasing threshold curve in arbitrary units. The pump rate corresponds to the pump fluence in the experiment, up to a scaling. A fit to experimental threshold curves can then be found by independently scaling the magnitude of the simulated signal and the pump rate. The scaling is done for one of the threshold curves, and the same scaling is used subsequently for the other. The shape of the curve is controlled by β and τ_{cav} of the modes, so by matching the shapes of the curves while using τ_{cav} from FEM simulations, an estimate of β can be found. The experimental curves flatten below a pump fluence of 48 μJ/cm^2 because there the signal from the SLR mode is below the broad spontaneous emission from the molecules (this starts to be evident in the lowest panels of Fig. 1(c) in the main text). Thus the theory and experimental threshold curves cannot be compared at those low fluences. At high pump fluences, the more flat behaviour of the experimental curves is due to photo-bleaching of the molecules at high pump intensities. This fit illustrates how 2% difference in β can lead to the experimentally observed effect. Moreover, it shows the correct order of magnitude for β; β-factors of different orders of magnitude yield poor fittings.

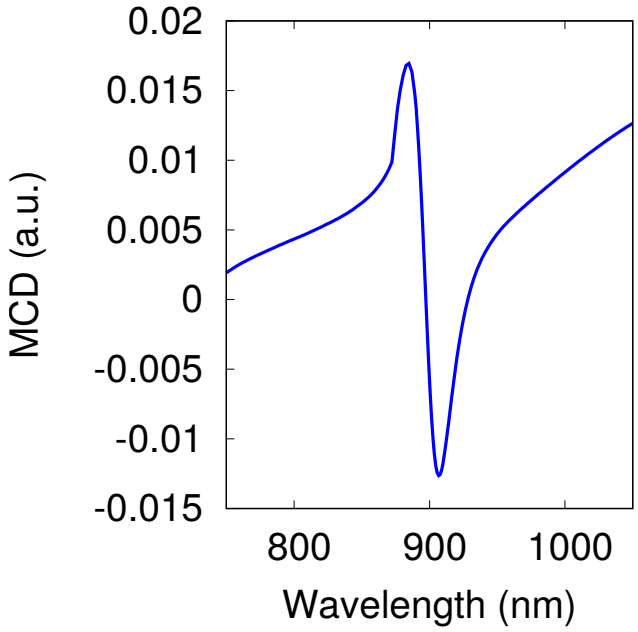

FIG. 12. Finite element method (FEM) simulation of the MCD spectrum of a square array of Co/Pt nanodots on top of a Au(150)/SiO_2(20) bilayer. The MCD effect is defined as the difference in reflectivity for σ^+ and σ^- light for magnetization pointing up (unnormalized, in arbitrary units). The shape of the MCD spectrum is similar to the experimental data shown in Fig. 1(b) of the main text.

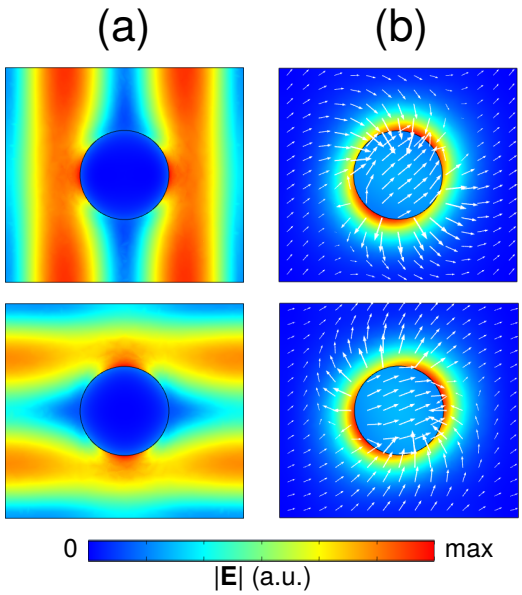

FIG. 13. Analysis of the modes sustained by the rectangular lattice. The electric field norm is shown for one unit cell at an XY-plane intersecting the nanodot at its mid-height. The case $p_x = 590$ nm and $p_y = 530$ nm with nonzero perpendicular magnetization is presented. We have found similar modes for the other rectangular arrays considered in the experiments. The electric field profiles of non-magnetized modes are analogous to those found in Supplementary Fig. 6(a)-(c). (a) Out-of-plane SLRs of the rectangular lattice. As a result of the x-y degeneracy lifting compared to the square lattice, the modes appear at clearly different energies: 1.390 eV (wavelength 892 nm) with linewidth 0.011 eV (upper panel) and 1.510 eV (wavelength 821 nm) with linewidth 0.009 eV (lower panel). Since these modes are linearly polarized in the $y-$ and $x-$directions, we have not found a well defined chirality. (b) In-plane hybrid modes of the rectangular lattice. Arrows in panels (b) depict the vectorial electric field: $\mathbf{E} = (E_x, E_y)$. Interestingly, magnetized modes in this configuration also appear with a well defined chirality. In particular, as in the square lattice, we found that the higher energy mode (upper panel) at 0.991 eV (wavelength 1253 nm) with linewidth 0.247 eV, features a σ^+ polarization, whereas the lower energy mode at 0.981 eV (wavelength 1266 nm) with linewidth 0.255 eV (lower panel), is σ^- polarized. We found $|C_{\sigma+}|^2 = 0.98$, $|C_{\sigma-}|^2 = 0.03$ for the higher energy mode and $|C_{\sigma-}|^2 = 0.99$, $|C_{\sigma+}|^2 = 0.02$ for the lower energy mode. The small numerical inaccuracies are due to the finite sized discretization of the analyzed geometry.

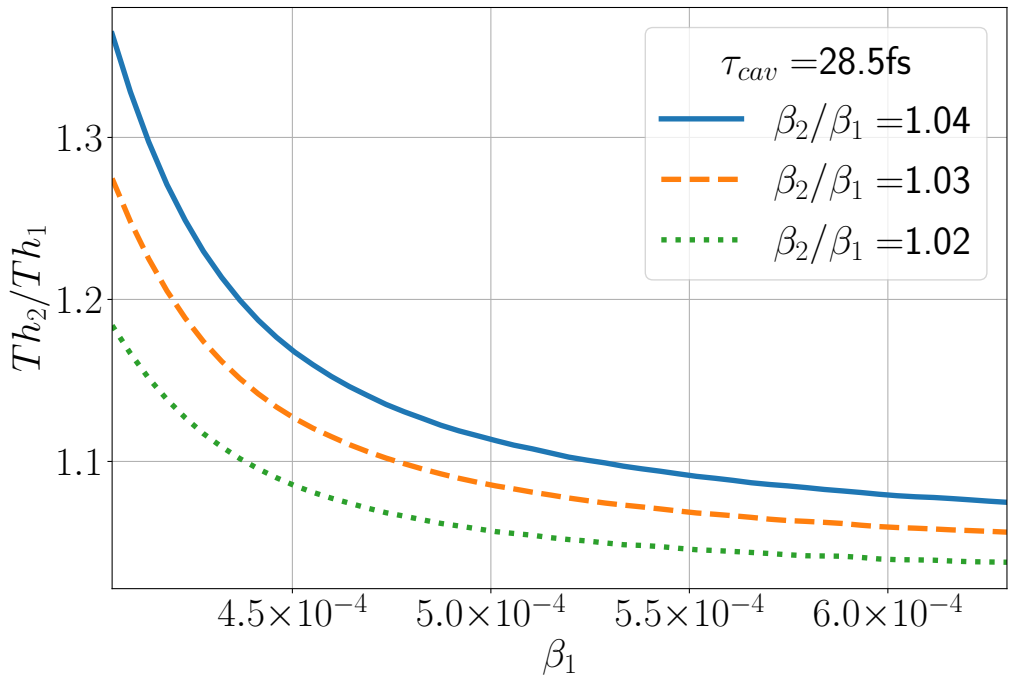

FIG. 14. Lasing threshold ratio, Th_2/Th_1, for one mode with a lifetime $\tau_{cav} = 28.5$ fs which can have two β-values ($\beta_{cav,1}$ and $\beta_{cav,2}$), as a function of $\beta_{cav,1}$. This corresponds to the case of the rectangular array where the lasing mode is always y-polarized while its β-factor can be chirality-dependent due to gain competition with the chiral hybrid modes. The lifetime is given by the FEM simulations of the lasing mode in the rectangular array (Fig. 13(a)) and the lasing threshold is defined as the pump rate, r, where the integrated lasing signal crosses 1% of the highest calculated integrated signal (see rate equation analysis in Methods). A 2-4% change in the β-factor results in a 5-26% threshold change for β-values in the range of $\beta \in [4.2, 5.5] \times 10^{-4}$.

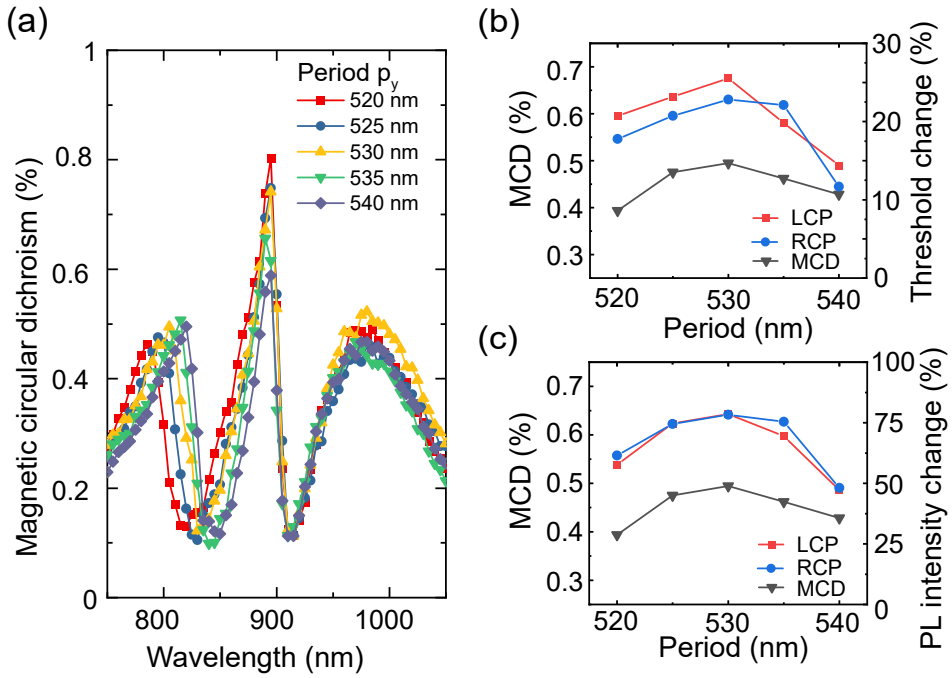

FIG. 15. (a) Magnetic circular dichroism spectra of rectangular Co/Pt nanodot arrays on top of a Au(150)/SiO_2(20) bilayer. The figure shows experimental data for arrays with $p_x = 590$ nm and p_y varying from 520 nm to 540 nm in 5 nm steps. The rectangular arrays show prominent features at the SLR wavelength determined by p_x (~ 890 nm) and the SLR wavelength determined by p_y (around 800 nm). (b),(c) Correlation between the MCD effect at 800 nm (pump wavelength in lasing experiments) and magnetic-field induced changes in (b) the lasing threshold and (c) the lasing intensity in saturation.

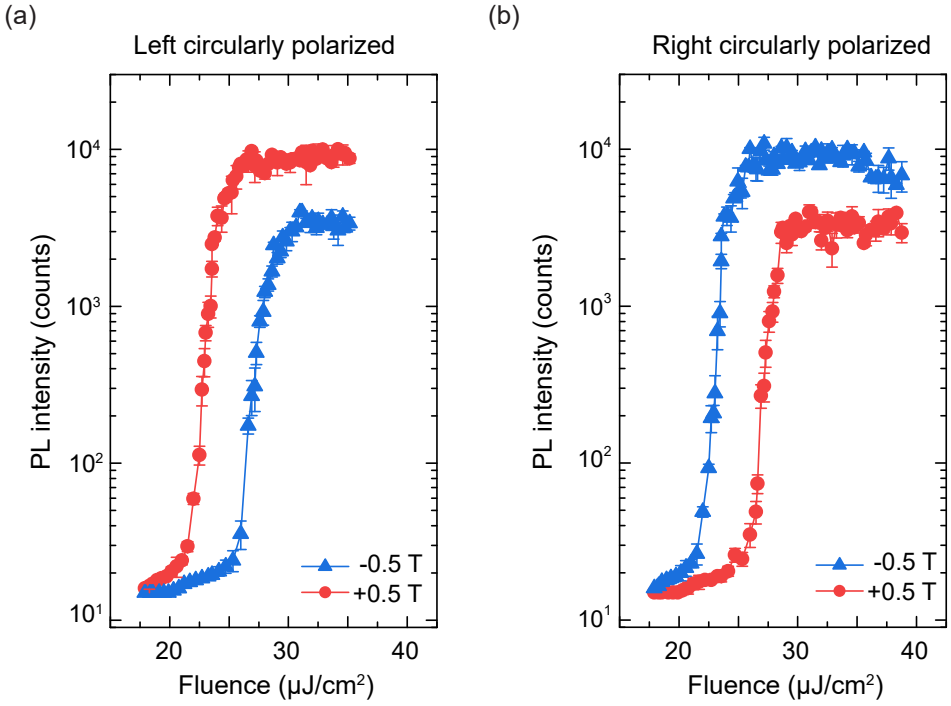

FIG. 16. PL intensity as a function of pump fluence for a Co/Pt nanodot array with $p_x = 590$ nm and $p_y = 520$ nm recorded under (a) σ^- and (b) σ^+ excitation.

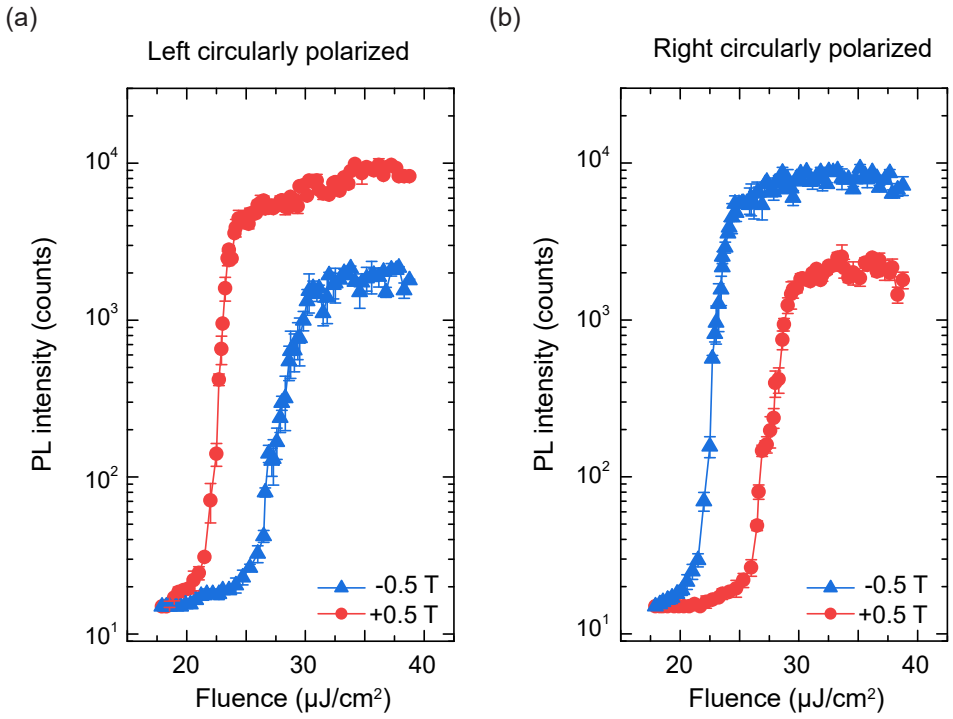

FIG. 17. PL intensity as a function of pump fluence for a Co/Pt nanodot array with $p_x = 590$ nm and $p_y = 525$ nm recorded under (a) σ^- and (b) σ^+ excitation.

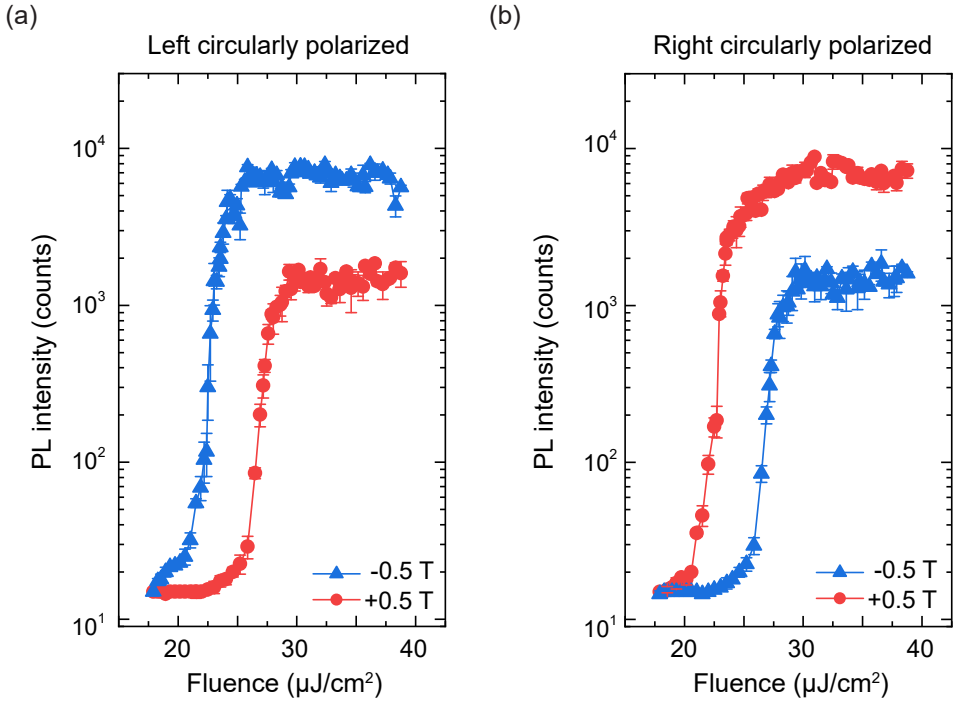

FIG. 18. PL intensity as a function of pump fluence for a Co/Pt nanodot array with $p_x = 590$ nm and $p_y = 530$ nm recorded under (a) σ^- and (b) σ^+ excitation.

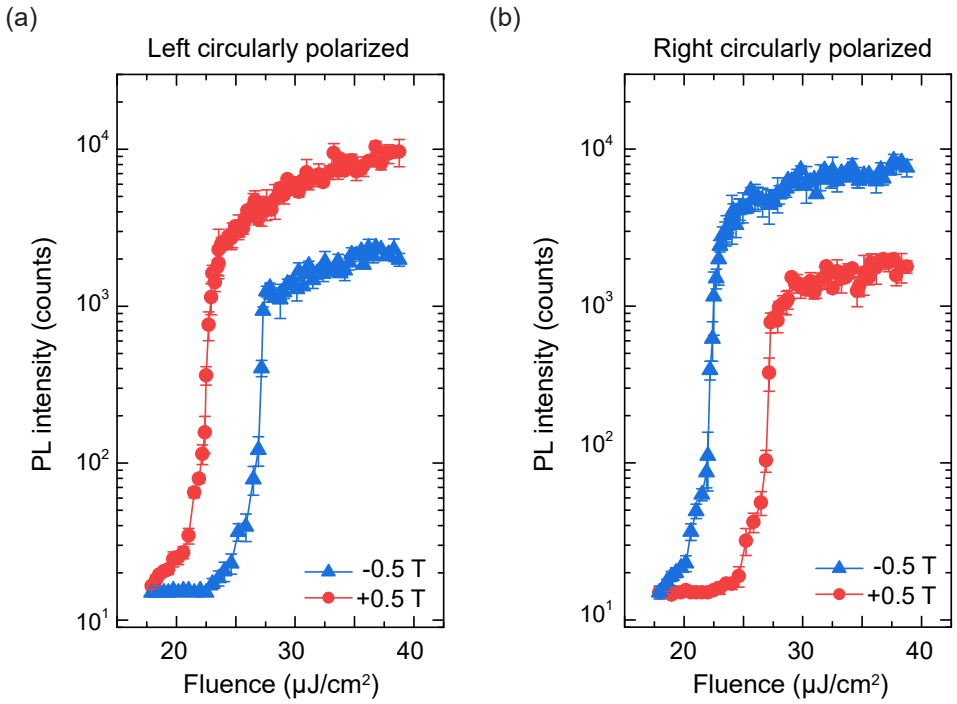

FIG. 19. PL intensity as a function of pump fluence for a Co/Pt nanodot array with $p_x = 590$ nm and $p_y = 535$ nm recorded under (a) σ^- and (b) σ^+ excitation.

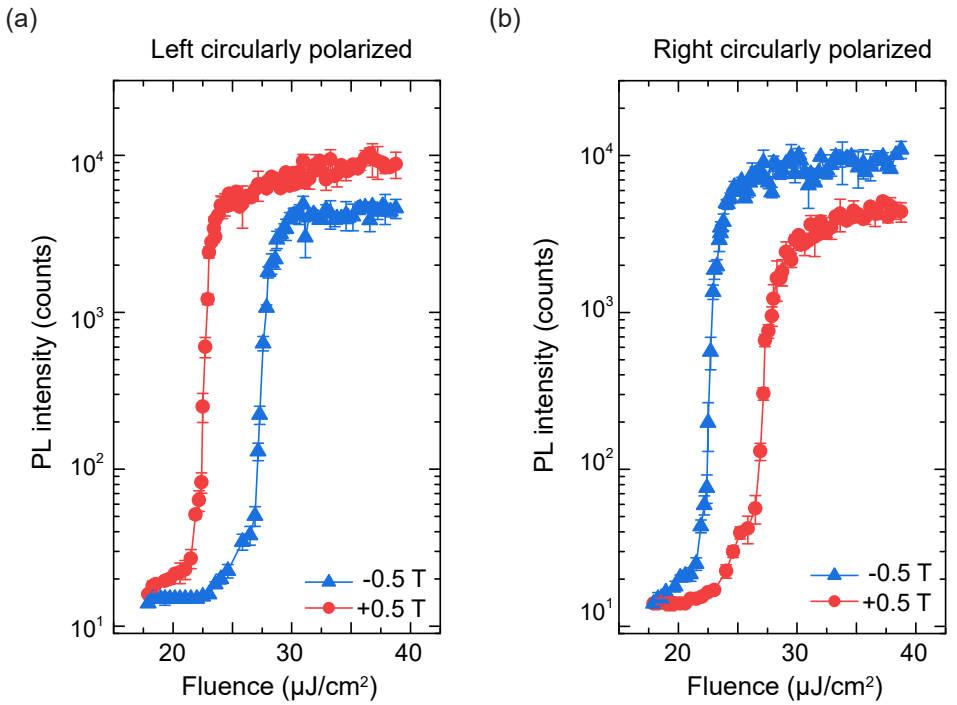

FIG. 20. PL intensity as a function of pump fluence for a Co/Pt nanodot array with $p_x = 590$ nm and $p_y = 540$ nm recorded under (a) σ^- and (b) σ^+ excitation.